Title

The hard x-ray nanotomography microscope at the advanced light source

Journal

Review of Scientific Instruments, 93(2)

ISSN

0034-6748

Authors

Nichols, Joseph B
Voltolini, Marco
Gilbert, Benjamin
et al.

Publication Date

2022-02-01

DOI

10.1063/5.0076322

The Hard X-ray Nanotomography Microscope at the Advanced Light Source

Joseph B. Nichols[†§], Marco Voltolini[‡], Ben Gilbert[‡], Alastair A. MacDowell[†], Michael Czabaj[§]

† Advanced Light Source, Lawrence Berkeley National Lab, Berkeley, CA 94720

§ Department of Mechanical Engineering, University of Utah, Salt Lake City, UT 84112

‡ Earth and Environmental Sciences Area, Lawrence Berkeley National Lab, Berkeley, CA 94720

Abstract

Beamline 11.3.1 at the Advanced Light Source is a tender/hard (6-17 keV) X-ray beamline recently re-purposed with a new full-field, nanoscale transmission X-ray microscope (nTXM). The endstation is suited to 50-250 μm samples of (generally) non-biological materials and has a theoretical resolution of 55 nm. The microscope is used in tandem with a 25 nm eccentricity rotation stage for high-resolution volume imaging using nanoscale computed tomography (nCT). The system also features a novel bipolar illumination condenser for the illumination of a ~100 μm spot of interest of the sample, followed by a phase-type zone plate magnifying objective with a ~52 μm field of view, and a phase detection ring. The zone plate serves as the system objective and magnifies the sample with projection onto an indirect X-ray detection system, consisting of a polished single crystal CsI(Tl) scintillator and a range of high-quality plan fluorite visible light objectives that in turn project the final visible light image onto a water-cooled CMOS 2048x2048 pixel[2] detector. Here we will discuss the salient features of this instrument, and describe our initial efforts to experimentally observe the internal 3D micro- and nanostructure of some highlighted materials, including composites and rocks.

Introduction

A consortium comprising the University of Utah Composites Laboratory, the Lawrence Berkeley National Laboratory (LBNL) Earth and Environmental Sciences Area (EESA) and the Advanced Light Source (ALS) have deployed a hard x-ray full field nano-tomography instrument. This microscope is capable of generating nanoscale, 4D image data of both high and low density materials with the assistance of novel *in-situ* environmental sample cells that can apply realistic environmental stresses.

Transmission X-ray microscopy (TXM) has long been used to image internal structure in an array of materials.[1] This is a consequence of the penetration of X-rays through materials, which has been exploited

in a variety of ways over the years.[2] One such application of a TXM system is to couple it with a rotational sample stage, such that 3-D internal volumes can be generated mathematically from a series of 2-D sample projections taken with a common center of rotation.[3–5] This has been employed to great effect in materials science research and development, with several notable micro-scale computed tomography (μCT) beamlines operating around the world.[6–11]

Typical μCT systems image direct projections using rectilinear propagation from the sample to detector, where the spatial resolution of the scintillator detector is limited to 0.5 – 1.0 um by depth of focus issues [12] associated with the visible light optical microscope objectives used to project the scintillator image onto a pixelated detector. NanoCT systems typically require x-ray zone plates as these optics, when fabricated to modern standards, have inherently higher spatial resolution compared to scintillators used in μCT systems. The zone plate projects its magnified image either directly onto the pixelated detector if a long path length of several meters is available or onto a scintillator with subsequent visible light magnifying optics if the path length available is short. Our 3 m long hutch constrains us to use the latter scintillator + x-ray zone plate technology.

Synchrotron-based tomography provides i) excellent temporal resolution afforded by the high photon flux, and ii) energy selection from a polychromatic source. Since the first reviews on synchrotron-based nano-tomography started appearing in the mid-2000s,[13,14] there has been a steady, forward march towards highly sophisticated X-ray optical systems, nano-fabrication techniques, and computational advancements.[15–18] These days, most synchrotrons are operating high-profile nCT beamlines, with several notable programs.[19–25] High-resolution radiography and nCT have opened up the materials sciences to observation of a whole new class of physicochemical processes at the nanoscale, and is still growing as a technique.[26] Beamline 11.3.1 folds into this nCT effort, as an improvement of resolution over the μCT facility that the local ALS materials user community have used to date on Beamline 8.3.2.[6]

Beamline Overview

The 11.3.1 end station was originally commissioned in 2004 as a small molecule crystallography beamline.[27] That experimental end station has moved elsewhere in the ALS, leaving a warm bend magnet source with a functional front-end setup. Bend magnets beamlines are often considered a low cost resource at most synchrotrons and have been shown to provide suitable illumination for full field transmission microscopy.[28] To this end, the nCT program took up residence at the vacant beamline, which

is serviced by a 3m long experimental hutch and warm-bend source focused to a monochromatic spot at the sample position. The energy selection range of 6-17 keV with the existing Si<111> monochromator is ideal for dense materials at the nanoscale, such as rocks and composite materials. The novel feature of 11.3.1 is not the high resolution but the fact the energy is sufficiently high (>10 keV) to pass through small but realistic environmental sample cells. The tight spot size of around 100 μm waist size (*h*x*v*) and high synchrotron flux are ideal for full-field dynamic imaging of 50-100 um samples.

General Layout

The major primary and microscope optics at 11.3.1 are shown in the layout of **Figure 1**. The source is a warm bend dipole magnet (1.9 GeV, 1.27 T, 500 mA) from the x.3 port of the ALS lattice with a source size of 95 x 17 μm full width half maximum (FWHM) (*h*x*v*). Brightness is in the range of 10^{16} ph s^{-1} $mrad^{-2}$ mm^{-2} 0.1% BW^{-1}, and the beamline accepts a divergence of up to 2.75 mrad x 0.25 mrad (*h*x*v*) as selected by adjustable apertures. The downstream components begin with a double Be window (5m) separating the machine and beam-line vacuum, followed by a cryo-cooled channel-cut Si<111> monochromator (6.5m). The monochromatic light is then directed onto a toroidal mirror (7m), which focuses the source through a Be window (13.7 m) to the sample position in the hutch (14m from source). The toroid focuses in the 1:1 configuration to reduce aberrations. The microscope is housed in the X-ray hutch, and is comprised of a condenser located just after the Be window, sample stage, zone plate, and indirect X-ray detection system. Each part will be described in more detail below.

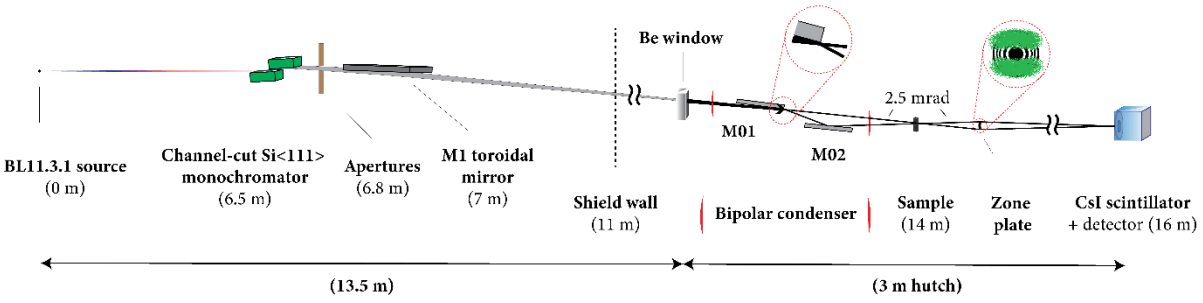

Figure 1. General schematic of the layout at beamline 11.3.1. The major optical components are specified along with their distance from the source.

Monochromator

The monochromator is a channel-cut Si<111> system with an energy selection range of 6-18 keV and an energy resolution of ~ 1000 as determined by the vertical acceptance of 0.25 mrad. The internal portion

of Si(111) monochromator is shown in **Figure 2**, alongside the flux energy spectrum, as measured by a calibrated Si pin diode. The top and bottom surfaces of the channel cut crystal are separated by 3 mm and have an acceptance of 3.0 mrad x 0.25 mrad (*hxv*). The top crystal surface is cut with a 0.28˚ offset that reduces vertical beam translation during rotation, which eliminates the need to realign with energy change.[27] The heat load on the monochromator is 17.5 W at 500 mA ring current. The cooling system is a cryogenic Joule-Thomson refrigerator that provides a base temperature of -173 °C but rises to -147 ˚C with the beam, this being the approximate point for zero thermal expansion of Si,[29] thus ensuring suitable transmission and stability of the monochromator. The channel cut monochromator is mounted with an Indium foil thermal interface on a Si cooling plate that is in turn thermally connected to the copper cold head, also via an Indium thermal foil. The monochromator rotation angle (energy selection) is afforded by a motor control system driving a differential rotary vacuum seal. Additional motors adjust the M1 tangential bend, roll and yaw.

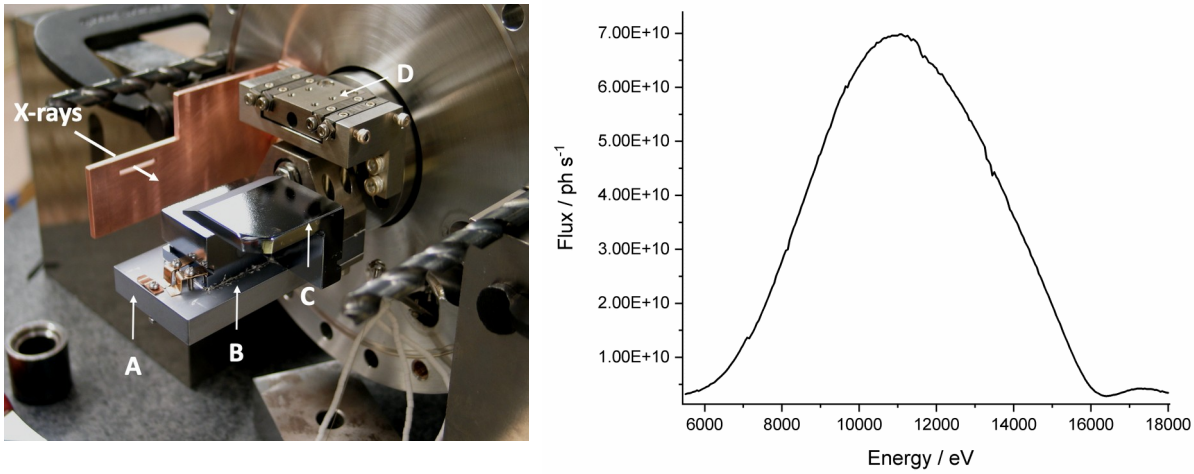

Figure 2. (Left) Photograph of Si<111> monochromator with internal components a) silicon base, b) indium foil thermal joint, c) Si<111> channel-cut crystal, and d) linear slide to manage thermal contraction of the cold head (Right) flux output of the beamline as measured at the sample position by a calibrated PIN diode.

The Mirror - M1

The source is imaged directly to the sample position (14m) by an M1 toroidal focusing mirror at 7m from the source operating in the 1:1 magnification geometry that reduces optical aberrations. The M1 mirror size limits the useful beamline acceptance to 2.5 mrad x 0.25 mrad (*hxv*). The focused spot is 96.1 μm x 107.8 μm at FWHM (*hxv*), as measured by computing the differential of an advancing knife-edge scan.

Comparison to the source FWHM (94.9 µm x 16.7 µm) indicates there is a sizeable vertical increase at the focus, due to a tangential slope error of ~ 3 µrad rms of the mirror.

The mirror itself is a bent silicon sagittal cylinder coated with a bilayer of 50 Å rhodium on top of 300 Å of platinum, with a surface roughness R_h of < 10Å. The incident angle is 4 mrad, which results in a high energy cut-off of ~18 keV. The beam is deflected downward at an angle of 8 mrad from horizontal. The mirror physical dimensions are 400 mm long, 40 mm wide, and 50 mm thick, with a 28 mm cylindrical sagittal radius. The mirror is tangentially shaped with a motorized "S" spring bender style mechanism,[30] and steered with 2 motors, that control the mirror's vertical angle (pitch) and yaw. The whole construct is immediately preceded by horizontal and vertical apertures, allowing for remote adjustment of X-ray beam vertical and horizontal acceptance.

The Hutch and Optical Table

The microscope itself is housed within a 3.0 m x 1.2 m steel experimental hutch (13.5m from source). The optical components are all mounted on a 0.61 m x 2.13 m optical breadboard. Vibration issues can lead to blurring and decrease effective resolution in 3-D volumes. The breadboard is in-turn mounted onto a 2500 kg Zanite block, - a quartz-resin composite. The Zanite block is placed on eight, 5 cm thick 16.5 cm OD Sorbothane (polyether-based polyurethane) dampers that convert vibrations to heat. The natural vertical frequency of the instrument is calculated at 8.5 Hz meaning that all higher frequencies transmitted via the floor are significantly damped. The whole instrument, being supported on visco-elastic dampers is not fixed, however the repositioning accuracy of the table structure is < 10 µm after minor displacement due to for example a user leaning against the table. This is adequate positioning stability being < 10% of the of the incoming x-ray beam focus size of ~ 100 um.

The Nanotomography Endstation

Hard X-ray nTXMs record 2-D projections of density distribution (absorption) and interface maps (phase) of the internal structure of dense materials. Coupling such a system to a high-resolution rotation stage allows for acquisition of the half-rotation projection series required to reconstruct 3-D images of the internal structure using a conventional tomographic reconstruction approach. At the micro-scale, TXMs are simple, direct projection systems with a detector system capable of micro imaging.[31] At the nanoscale level, the projection image of the sample requires magnification to achieve nm imaging resolution. Typically this requires high resolution zone plates made with frontier nanoscale manufacturing that have

only become available in the last decade given the high aspect ratio feature size required for hard X-rays.[32] The following section is a description of the microscope and the employment of modern X-ray opto-mechanical systems for transmission imaging and CT.

The model of the 11.3.1 microscope is shown in **Figure 3**. The path of the X-rays through the endstation can be summarized as follows. Monochromatic light leaves the beryllium window (a) 34 cm upstream of the sample position. The illumination is immediately shaped by a condenser (b) to yield 2.5 mrad (*hxv*) of converging illumination aimed at the sample (d) and focused to ~ 100um spot. An x-ray projection is generated by the sample, which is magnified by a zone plate objective (e) onto the scintillator-detector system (g, h).

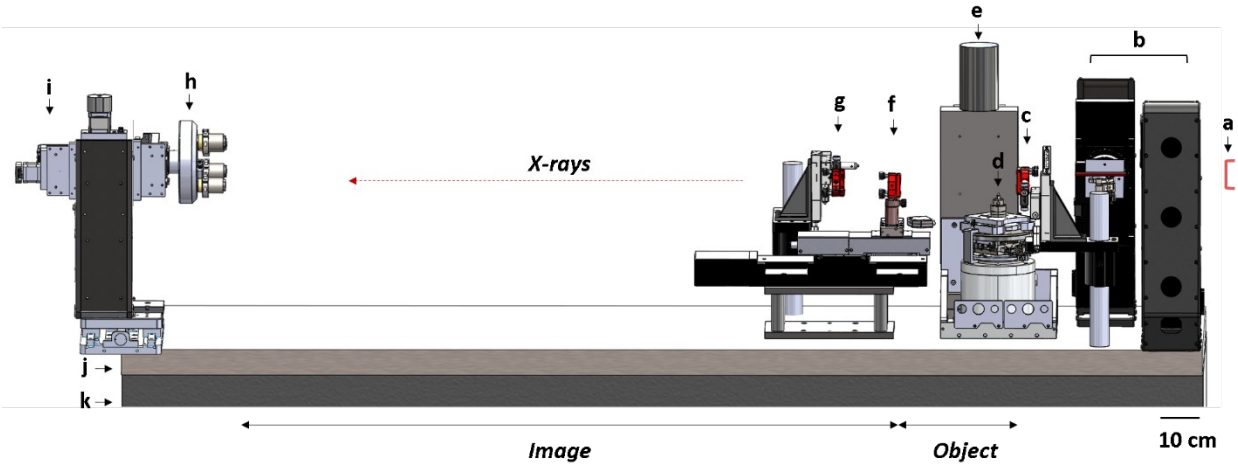

Figure 3. Model of nTXM at beamline 11.3.1. Components are listed as follows: a) beryllium vacuum window, b) bipolar illumination condenser, c) pinhole, d) sample mount, e) sample stage, f) zone plate, g) phase ring, h) scintillator-visible objective turret, i) water-cooled 2048 x 2048-pixel visible detector, j) breadboard, k) Zanite mounting table. X-ray path shown as dotted arrow.

The Zone Plate

Sample magnification of X-rays is accomplished with a diffractive optic called a Fresnel zone plate, used here as an X-ray analog to a typical visible light microscope objective. The zone plate acts as a variable period diffraction grating where alternating concentric zones of phase shifting material result in constructive interfere at the desired focus.[33] This is a 2-D approximation of an ideal X-ray lens, which works in much the same way as a standard thin optical lens, with *n* order focal points ($f_1 ... f_n$) and a real image plane distance specified by the thin lens equation.

Zone plates are specified by consideration of 3 parameters; the incident photon energy, the resolution as set by the outer zone width Δr_M, and the number of zones N which defines the required spectral bandwidth, $\lambda/\Delta\lambda$. An array of consequential parameters, relating focal length, depth of field, wavelength, etc. follows from these.[34] The zone plates in use at 11.3.1 all have a Δr_M of 40 nm and range of diameters from 105 – 255 μm. They are Au electroplated in a 2x2 array on 50nm thick Si_3N_4 membrane, as shown in **Figure 4** (left).

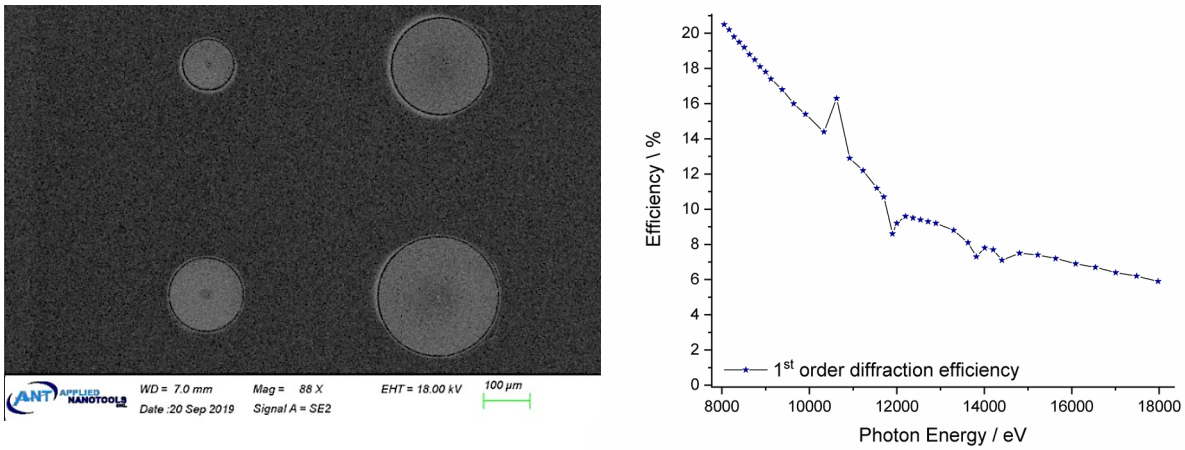

Figure 4. Left **-** Scanning electron microscope images of zone plates in use at 11.3.1. There are 4 zone plates of sizes 105, 155, 205 and 255 μm with 654, 966, 1284, and 1596 zones, respectively. (Right) calculated zone plate efficiency for the 155 μm diameter plate *vs.* incident photon energy. Data and zone plates supplied by manufacturer Applied Nanotools, Saskatchewan, Canada.

The thickness of the Au for optimal π phase shift at 12 keV is 2.49 μm which corresponds to an aspect ratio of 62 for the outermost ring. This is not feasible with current zone plate technology. A compromise between diffraction efficiency and resolution is required. The zone plates have a practical Au thickness of 0.92 μm with an outer zone width of 40 nm, giving an aspect ratio of 23. This corresponds to a 1st order efficiency of 17.8% at 9 keV **Figure 4** (right). They were designed such that the acceptance (input 2NA = ~2.5mrads) match the convergence of the x-rays illuminating the sample.

The working distance of such a setup allows for the incorporation of environmental cells. For the 155 um diameter zone plate (N=966) the sample to zone plate = 62 mm at 12 keV. The magnification is limited to 23 by the short hutch length, which restricts sample to detector distance to 1500 mm. The FOV of the zone plate is calculated at 52 μm and mapped onto the 2048x2048 pixels[2] detector, such that the pixel size

represents 25 nm. This implies a Nyquist resolution of 50 nm, matched suitably to the system resolution set by the ZP outer zone width, Δr_M = 40nm. The ~ 100 μm beamline focused spot size allows for over-filling of the 52 μm FOV, leading to uniform sample illumination. The zone plate input 2NA is 2.475 (at 12 keV), resulting in a good illumination match from the 2.5 mrad horizontal convergence from the beamline, but is under-filled by the 0.25 mrad vertical beamline convergence when no condenser optics are used between the beamline and sample. This is addressed by a suitable condenser system.

Condenser Illumination System

There are, in general, 3 options for reflective condenser systems in an nTXM – capillary condenser, Kirkpatrick-Baez (KB) mirrors, or a multi-pole configuration. The illumination used at 11.3.1 is the latter - a two-mirror system allowing for adjustable NA. This form of novel bi-polar illumination is used in lieu of a formal light shaping system, such as the former two – the capillary or KB condensers. Micro-pulled, ellipsoidal capillaries are known to reliably focus synchrotron radiation to a ring of annular illumination with a backstop.[35] Capillaries generate the desired annular illumination, but are of fixed NA, fixed FOV, and are generally cost-prohibitive, restricting the ongoing adaptability of the system. KB mirrors, on the other hand, are a pair of grazing-angle elliptical X-ray focusing mirrors capable of more dynamic illumination control.[36] These mirrors simultaneously focus the horizontal and vertical of the beam at the sample position, accomplished while working as an orthogonal pair with a typical focal length allowing for several centimeters of working distance to the sample. KB's provide uniform illumination with the appropriate divergence for adequately filling the zone plate. KB's are however expensive to manufacture and require complicated motor control systems.

For this work we adopted the use of a two plane-mirror configuration, as shown in the schematic in **Figure 1.** It crudely part -approximates the annular output shape of a capillary and matches the vertical convergence of the radiation onto the sample to be the same as the horizontal. This is done by splitting the single beam entering the hutch into two with a dual reflection condenser scheme. The silicon mirrors used are flat to < 1 μrad rms, 0.2 nm rms roughness with 25 nm Pt coating (supplier – General Optics) that are 102 mm long x 12.5 mm wide x 5 mm thick, with a beam footprint along the optical axis of approximately 40 mm.

The full-width beam leaves the Beryllium window and the top half of the beam is reflected downwards by M01 at 2.5 mrad grazing angle. The lower portion of beam travels through to the focal point at the sample and partially fills the bottom half of the zone plate. The upper portion after reflection from M01 and M02 overlaps with the straight through light at the sample position, and then partially fills the top half of the

zone plate. The resultant bipolar optical filling of the zone plate is shown in a zoom insert of **Figure 1**. This bipolar illumination approximately matches the annular illumination achieved by that of a capillary condenser and suggests similar quality images can be obtained by the different condenser techniques. The illumination of the sample position and the filling of the zone plate can be tuned by rotating and translating the mirrors with respect to the reflection geometry to alter the illumination convergence angle in the vertical. The horizontal convergence angle is controlled by apertures upstream of the M1 toroid that effect the horizontal beamline acceptance. Development is still ongoing, as preliminary studies show that slight dithering of the mirrors further reduce coherent artifacts in the image. The current condenser though can only dither half the x-rays reflected by the mirrors. Adding more mirrors will allow for more control over this coherent illumination aspect of this illumination type.

The condenser requires a scatter management aperture upstream of the sample to reduce errant light from the wings of the ~100um focused spot on the sample. Overfilling the sample FOV has the advantage of more uniform illumination, but suffers from additional photons outside the 52 μm FOV, which increases the background signal, reducing contrast at the image plane. Raytracing indicates the background can be suppressed by the addition of a 70 μm pinhole placed 10 mm upstream of the sample. We use an array of pinholes from 50-250 μm and select one to match the system with the type of sample. This reduces the background, but compromises the working distance. In an effort to circumvent this issue, additional work is ongoing to characterize the pinhole position versus contrast trend.

Sample Stage

The discovery of the Radon transform in the early 20th century lead to the ability to calculate 3-D structure from 2-D projections taken at multiple angles between 0-180°.[3,4] The leap to tomography from transmission microscopy is enabled by the use of a high-resolution rotational sample stage. The in-line rotational sample mount at 11.3.1 is an air-bearing with a radial and axial accuracy of 0.025 μm and a tilt accuracy of 0.012 μm per 25 mm. (AB Tech Inc). The rotational encoder provides 4.74E6 counts/revolution, indicating a 7.5E-5 degree of positional resolution. A variety of convenient sample mounting systems, including small substrates and vices, can be mounted rigidly on quick-release plates that mount on kinematic bases. The kinematic bases are in turn mounted on an XY stage for center positioning using orthogonal high-resolution micro-stepper motors. Sample alignment is initially accomplished with two orthogonal cameras equipped with zoom lenses followed by image centralization on the final detector camera.

Sample Materials

There are two contrast scenarios for generating a sample image with nTXM, the phase-shift (edge-detection) and absorption (intensity contrast) cases, as set by the real and imaginary parts of the complex index of refraction, respectively. Hence, the contrast generated at the detector depends on the atomic makeup of the material and the operating energy.[37] The plots of the complex index for low-Z Carbon (CMCs) and some example geo-materials (**Figure 5**), illustrate this concept. Carbon has a low absorption cross-section (F_2,β) of 0.01 at 10 keV, while Ca is almost 100x higher, meaning that geo-materials are candidates for absorption contrast. However, despite an almost negligible absorption response, the phase response (F_1,δ) of the carbon is significant, meaning reliable imaging of low-absorption CMC materials with phase imaging is feasible. This form of imaging is facilitated by the employment of an in-line phase detection system, to be described in a following section.

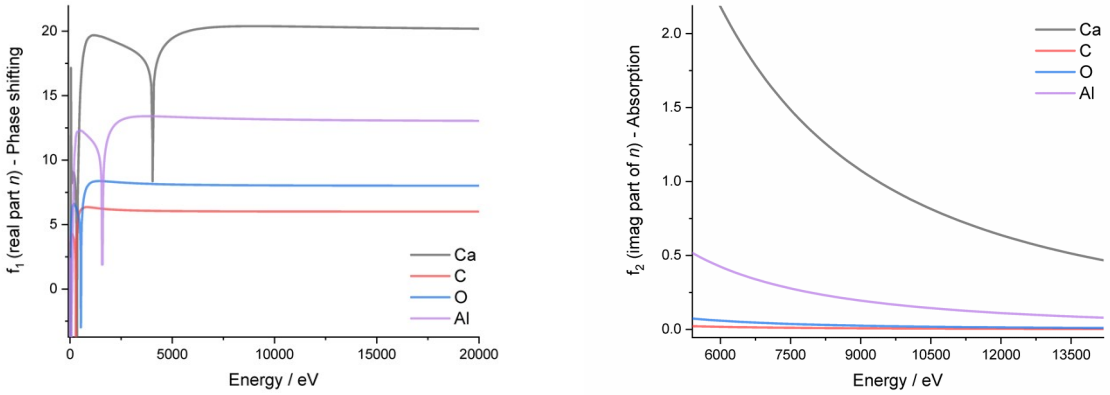

Figure 5. Plots of the real and imaginary parts of the index of refraction versus energy for typical sample materials.

Concerning sample preparation, the CMC samples are of a yarn-like, woven structure in their native state, requiring little to no sample preparation. The earth sciences materials, however, require particular method development. A Unipol 810 polishing tool is used to thin down sections of sample material using diamond slurry, from these sections, an in-house Oxford Lasers Class 3b 532 nm mill was used to etch out sample patterns, usually in the form of pillars cut to 50-200 μm diameter. The laser miller provides a 532 nm laser light focused to a 10 μm spot size with 50 mW power output.

Phase Detection System

The image formed at the real image plane has 3 light-based components: straight through light and light scattered by the two distinct contributions from the complex index of refraction, δ and β. The image is the superposition vector of the undiffracted ($\vec{U}$) and diffracted ($\vec{D}$) light. The undiffracted light is the image bright-field, and has no phase change after passing the sample. The diffracted light that is absorbed (β) undergoes a π phase shift and destructively interferes with the undiffracted light at the image plane leading to clear image contrast. $\overbrace{(U¿-\vec{D})}¿$. On the other hand diffracted light that is merely phase shifted (δ) typically undergoes ~ π/2 phase shift which when interfered with undiffracted light yields little destructive interference as the added orthogonal vectors ($\vec{U}+\vec{D}¿$ yield a similar magnitude as the undiffracted light and thus little contrast in the image plane.[38] The Zernike phase contrast approach to imaging phase objects is to shift the phase of the undiffracted light by π/2 or 3π/2. Contrast is achieved in the image plane as the vectors are aligned either constructively ($\vec{U}+\vec{D}¿$ or destructively $\overbrace{(U¿-\vec{D})}¿$.

The phase shifting of the undiffracted light is accomplished with the use of a Zernike phase ring, which requires the placement of a phase-shifting material at the back focal plane. The first order focal point sets the longitudinal ring position, which is set by the first zone in the objective (the back focal plane is located at $f = r_1^2/\lambda$). The phase ring OD is set to overlap the outer-edge of the bright-field projection cone, i.e. the light undiffracted by the sample ($\vec{U}$)**,** see **Figure 6**.[39] The undiffracted light is focused to the real image plane with an image convergence of Θ^{Image} (55 μrad for the 155 μm objective). This sets the outer diameter, whereas the inner diameter is generally set by convention at 0.8(OD). The phase rings are laser cut from 7 μm thick Au foil and mounted on 25 μm thick Kapton tape. The foil was chosen with the thickness required to phase shift the undiffracted light by ~ 3π/2.[40] The phase rings are mounted on motors for adjustment in the optical plane to maximize contrast. The rings are easily removed for absorption contrast by translation from the beam path.

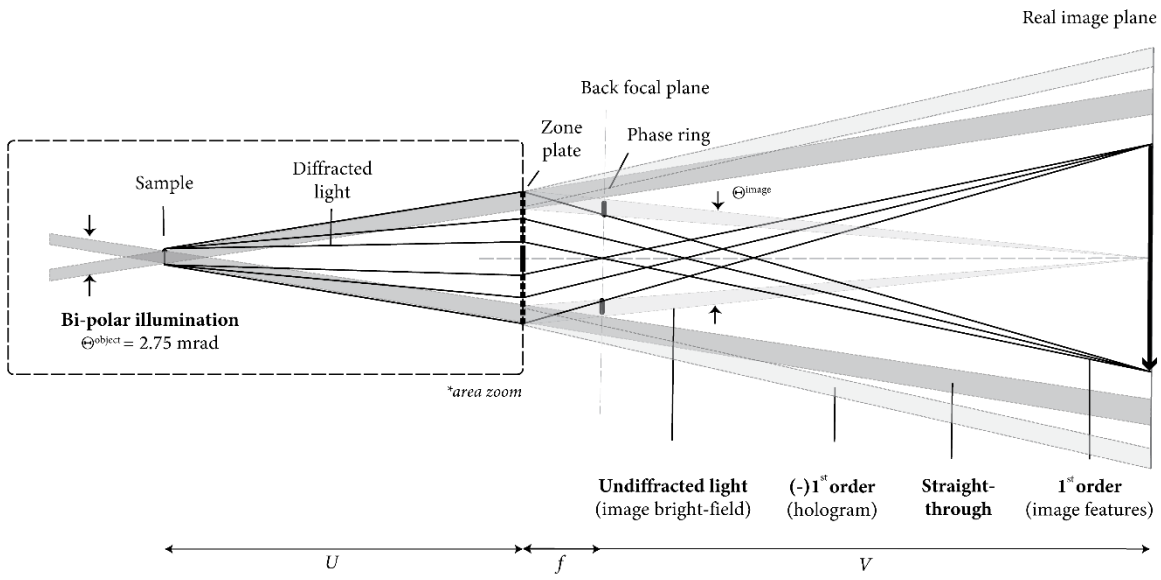

Figure 6. Schematic showing diffraction orders and general principle of operation of the zone plate objective in use at 11.3.1. The area in the dashed box is a zoom of the sample → zone plate path: the working distance (U) ≈ the focal distance (f), and the image distance (V) is such that V/U is the zone plate magnification, 13x-35x. Adapted from Chen *et al.*[41]

The Scintillator-Detection System

The final imaging system at 11.3.1 is an indirect X-ray detection system. The system is comprised of 3 components; the scintillator, a visible light objective, and the detector. The X-ray image created by the zone plate strikes the scintillator, which produces visible scintillated light proportional to the X-ray intensity. The scintillator employed is a Thallium activated Cesium Iodide single crystal (CsI(Tl)) mounted at the image plane of a high quality visible light objective. There are four objectives (2x, 4x, 10x, 20x) mounted on a microscope turret for ease of magnification change. Each objective carries a scintillator mounted behind either a thin Beryllium window or glassy carbon window to allow x-ray penetration but exclude external visible light. The CsI(Th) crystals are hygroscopic and are mounted hermetically. The CsI(Tl) scintillator has a light output of 54 photons/keV with peak output at 540nm and a FWHM of ~150nm, which overlaps the objective peak transmissivity (>80%).

The scintillated images are magnified by the visible objective, offering a range of pixel sizes from 250 – 25 nm. The depth of focus of the objectives must be matched to the scintillator thickness at maximum diffraction-limited resolution, which is 4.9, 2.08, 0.9, and 0.5 μm for the 2x-20x, respectively.[42] However, for the higher magnification visible objectives, the pixel size is smaller than the achievable resolution

from the zone plate, hence the DOF can be larger in proportion, resulting in more reasonably achieved CsI(Tl) thickness, i.e., 300 µm, 60 µm, 30 µm, and 10 µm, for the 2x-20x, respectively. This sets the requirement for the thickness of the scintillator, which must be weighed against the stopping power of the crystal, as seen in the transmissivity plot in **Figure 7**. The 400 µm thick, 12.7 mm diameter scintillators were of optical quality and were acquired from MTI Corporation and Sygray. Crystals that were thinned used a Unipol 810 polisher in conjunction with a Ted Pella thinning jig. A MicroCloth long-nap polishing cloth with a range of oil-based diamond slurries from 3 µm – 0.02 µm was used. The final step was a hand polish with a MicroTex synthetic silk cloth.

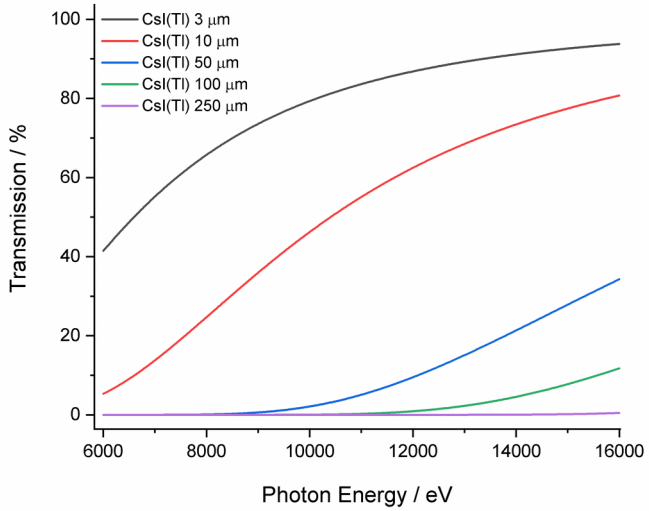

Figure 7. Graph of X-ray transmission percentage through CsI(Tl) scintillator versus photon energy for 3-250 µm thickness.

The scintillator system is coupled to a 2048 x 2048 pixel^2 sCMOS PCO Edge 4.2BI Peltier water-cooled detector (-25 °C) with a pixel size of 6.5 µm and active area of 13.3 mm x 13.3 mm. The detector has a dynamic range of 26667:1 and a spectral range of 370 nm – 1100 nm. The detector quantum efficiency (DQE) is reported at > 95%.

Initial Sample Imaging

Figure 8 shows a section through an IM7/8552 laminate channel-plate composite. The sample is comprised of 5 µm diameter carbon fibers embedded in epoxy. This reconstructed volume was taken at 9500 eV, with an exposure time of 3s per frame, 1024 projections over 180°, and in phase detection

mode. The projections were reconstructed using a typical filtered back projection routine. Slight ringing is present in the exploratory samples, and is thought to be associated with the illumination, indicating a need for further refinement. The carbon fibers and epoxy are of very similar density so amplitude contrast is weak. The phase imaging does clearly show the edges of the fibers despite the similar density of the 2 materials. Study of these new materials are often focused on failure mechanisms which are manifest usually as a defect in the internal structure such as a bubble of crack. The featureless nature of this slice is indicative of good filling by the epoxy. In the upper left there are indications of the start of a crack between 2 carbon strands. Further refinements in the sample preparation and sample tension jigs will examine such crack propagation.

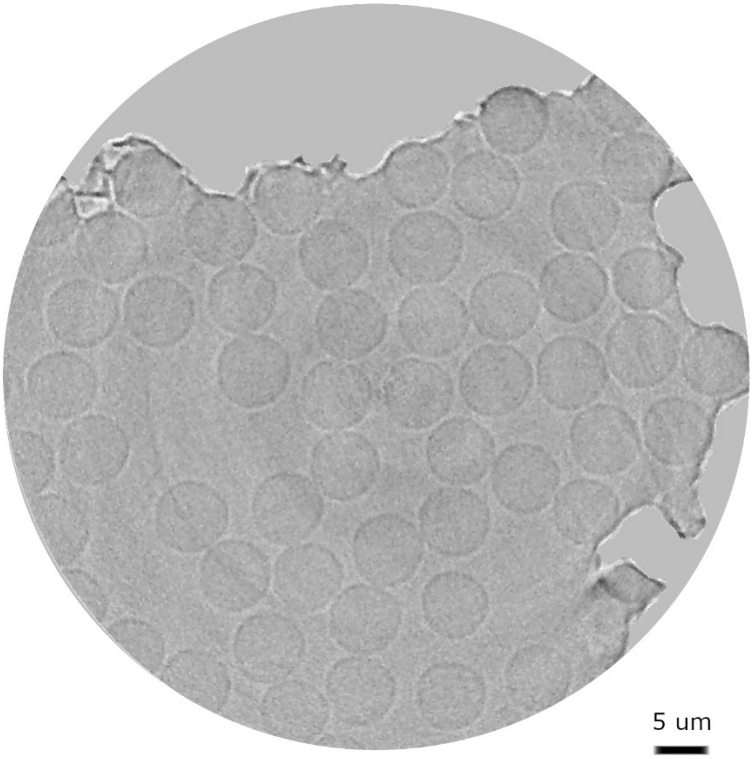

Figure 8. Mid-volume slice in reconstructed stack of IM7/8552 channel-plate laminate. Stack masked with flat background.

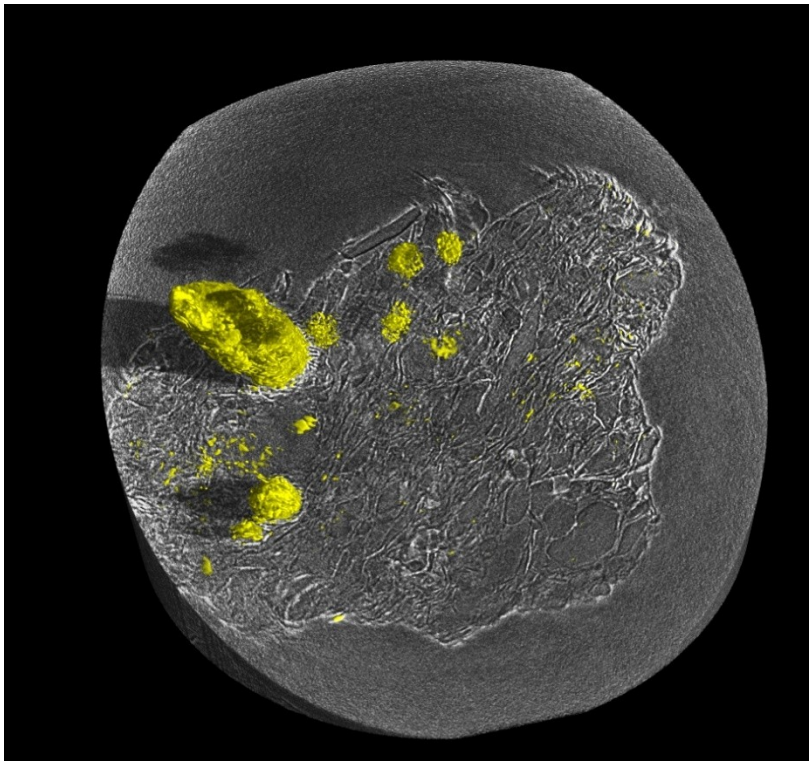

Figure 9. Volume reconstruction of a Green River shale with segmented Pyrite (framboids and fossils) in yellow, interfaces obtained using a filtered back projection method. Projections taken at 9639 eV, with an exposure time of 4s per frame, 1024 projections over 180°, and in absorption mode.

Future Work

(H. Lisabeth) A mechanical loading device has been developed in parallel with the beamline in order to perform in situ mechanical testing with concurrent imaging. The apparatus consists of a single loading column supported by a c-frame (**Figure 10**). Samples are fixed between two hollow, needle-shaped loading platens which are sealed to pipe fittings, allowing fluid to flow within the annulus between the sample and a polyimide jacket. Force is measured via an integrated donut-style load cell with a linear range of 0-10N. For a sample with a 40 micron circular cross-section, this amounts to an axial pressure range of more than 8 GPa. Three micrometers arranged orthogonally allow for coarse positioning of the platens while fine control is provided by a three-axis piezo-controlled stage (PI Nanocube). The stage is driven by a computer-integrated piezo controller (PI E-727) that allows arbitrary loading paths and direct feedback from the integrated load cell. This apparatus is designed for contact-scale mechanics studies in the presence of chemically reactive fluids and is well suited for single grain as well as grain-grain experiments. This data can be used to study the static elastic properties of granular materials as well as the onset of micro-plasticity and the role of chemistry on the grain scale.

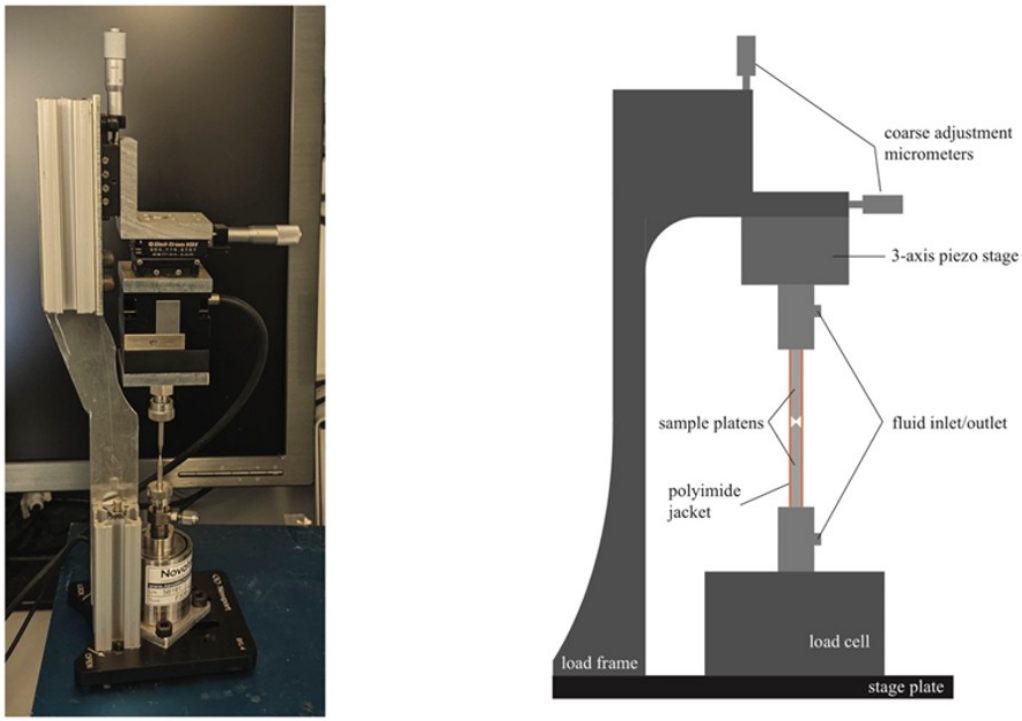

Figure 10. Nanomechanical loading device, (left) picture and schematic of the device and (right) and example of mechanical data from a constant displacement rate deformation experiment on a single calcite grain. (H. Lisabeth)

References

1. Kirz, J. & Jacobsen, C. The history and future of X-ray microscopy. in *J Phys Conf Ser* vol. 186 1–11 (2009).

2. Chapman, H. N. X-ray imaging beyond the limits. *Nat. Mater.* **8**, 299–301 (2009).

3. Radon, J. Über einige Fragen betreffend die Theorie der Maxima und Minima mehrfacher Integrale. *Monatshefte für Math. und Phys.* **22**, 53–63 (1911).

4. Ramlau, R. & Scherzer, O. The first 100 years of the Radon transform. *Inverse Probl.* **34**, 0–4 (2018).

5. Kalender, W. A. X-ray computed tomography. *Phys. Med. Biol.* **51**, 29–43 (2006).

6. Barnard, H. S. *et al.* Synchrotron X-ray micro-tomography at the Advanced Light Source: Developments in high-temperature in-situ mechanical testing. *J. Phys. Conf. Ser.* **849**, 0–6 (2017).

7. Carlo, D., Carlo, F. De, Xiao, X. & Tieman, B. X-ray tomography system, automation, and remote access at beamline 2-BM of the Advanced Photon Source. *Proc. SPIE* (2006) doi:10.1117/12.681037.

8. Stampanoni, M. *et al.* TOMCAT: A beamline for TOmographic Microscopy and Coherent rAdiology experimenTs. *AIP Conf. Proc.* **879**, 848–851 (2007).

9. Brun, F. *et al.* Enhanced and Flexible Software Tools for X-ray Computed Tomography at the Italian Synchrotron Radiation Facility Elettra. *Fundam. Informaticae* **141**, 233–243 (2015).

10. Di Michiel, M. *et al.* Fast microtomography using high energy synchrotron radiation. *Rev. Sci. Instrum.* **76**, (2005).

11. Uesugi, K., Takeuchi, A. & Suzuki, Y. High-definition high-throughput micro-tomography at SPring-8. *J. Phys. Conf. Ser.* **186**, 7–10 (2009).

12. Koch, A., Raven, C., Spanne, P. & Snigirev, A. X-ray imaging with submicrometer resolution employing transparent luminescent screens. *JOSA A* **15**, 1940–1951 (1998).

13. Withers, P. J. & Alexander Sasov. X-ray nanotomography. *SPIE 49th Annu. Meet.* **10**, 26–34

(2007).

14. Midgley, P. A., Ward, E. P. W., Hungría, A. B. & Thomas, J. M. Nanotomography in the chemical, biological and materials sciences. *Chem. Soc. Rev.* **36**, 1477–1494 (2007).

15. E. Di Fabrizio, D. Cojoc, S. Cabrini, B. Kaulich, T. Wilhein, 1 and J. Susini. Design and fabrication of new optics for X-ray microscopy and material science. *J. Phys. IV Fr.* **104**, 177–183 (2003).

16. Kaulich, B. *et al.* TwinMic: Combined scanning and full-field imaging microscopy with novel contrast mechanisms. *Synchrotron Radiat. News* **16**, 49–52 (2003).

17. Chang, C., Sakdinawat, A., Fischer, P., Anderson, E. & Attwood, D. Single-element objective lens for soft x-ray differential interference contrast microscopy. *Opt. Lett.* **31**, 1564–1566 (2006).

18. Tang, M. *et al.* Nano-Transmission X-ray Microscopy at NSRRC. *NSRRC* **15**, 241115.

19. Shen, Q. *et al.* Dedicated full-field X-ray imaging beamline at Advanced Photon Source. *Nucl. Instruments Methods Phys. Res. Sect. A Accel. Spectrometers, Detect. Assoc. Equip.* **582**, 77–79 (2007).

20. Bare, S., Liu, Y. & Nelson, J. W. Applications of Full-field Transmission X-ray Nanotomography and X-ray Nanospectroscopy at Stanford Synchrotron Radiation Lightsource. *Microsc. Microanal.* **26**, 778–780 (2020).

21. Ogurreck, M. *et al.* The nanotomography endstation at the PETRA III imaging beamline. *J. Phys. Conf. Ser.* **425**, (2013).

22. M. Stampanoni, F. Marone, P. Modregger, B. P. & T. Thüring, J. Vila-Comamala, C. David, R. M. Tomographic hard x-ray phase contrast micro- and nano-imaging at TOMCAT. *AIP Conf. Proc.* **1266**, 13–17 (2010).

23. Takeuchi, A., Suzuki, Y. & Uesugi, K. Present Status of the Nanotomography System at BL47XU at SPring-8 and Its Efficiency Improvement Using Double-Condenser Optics. in *AIP Conference Proceedings* vol. 1365 301–304 (American Institute of Physics, 2011).

24. Scheel, M. *et al.* Status of the tomography beamline at Synchrotron SOLEIL. **4**, 2017 (2018).

25. Ge, M. *et al.* One-minute nano-tomography using hard X-ray full-field transmission microscope. *Appl. Phys. Lett.* **113**, 83109 (2018).

26. Withers, P. J. *et al.* X-ray computed tomography. *Nat. Rev. Methods Prim.* **1**, 1–21 (2021).

27. Thompson, A. C. *et al.* A simple high performance beamline for small molecule chemical crystallography. *AIP Conf. Proc.* **705**, 482–485 (2004).

28. Feser, M., Howells, M. R., Kirz, J., Rudati, J. & Yun, W. Advantages of a synchrotron bending magnet as the sample illuminator for a wide-field X-ray microscope. *J. Synchrotron Radiat.* **19**, 751–758 (2012).

29. Shah, J. S. & Straumanis, M. E. Thermal expansion behavior of silicon at low temperatures. *Solid State Commun.* **10**, 159–162 (1972).

30. Howells, M. R. *et al.* Theory and practice of elliptically bent x-ray mirrors. *Opt. Eng.* **39**, 2748–2762 (2000).

31. Landis, E. N. & Keane, D. T. X-ray microtomography. *Materials Characterization* vol. 61 1305–1316 (2010).

32. Jefimovs, K. *et al.* Fabrication of Fresnel zone plates for hard X-rays. *Microelectron. Eng.* **84**, 1467–1470 (2007).

33. Kirz, J. Phase zone plates for x rays and the extreme uv. *J. Opt. Soc. Am.* **64**, 301–309 (1974).

34. Lawrence Berkeley Lab, U. Fresnel Zone Plate Theory. http://zoneplate.lbl.gov/theory.

35. Dozier, C. M., Newman, D. A., Gilfrich, L. V, Freitag, R. K. & Kirkland, J. P. Capillary Optics for X-Ray Analysis. *Adv. X-ray Anal.* **37**, 499–506 (1993).

36. Yamauchi, K. *et al.* Single-nanometer focusing of hard x-rays by Kirkpatrick–Baez mirrors. *J. Phys. Condens. Matter* **23**, 394206 (2011).

37. Willmott, P. *An Introduction to Synchrotron Radiation*. *An Introduction to Synchrotron Radiation* (2011). doi:10.1002/9781119970958.

38. Neuhäusler, U., Schneider, G., Ludwig, W. & Hambach, D. Phase contrast X-ray microscopy at 4 keV photon energy with 60 nm resolution. *J. Phys. IV* **104**, 567–570 (2003).

39. Zernike, F. Diffraction theory of the knife-edge test and its improved form, the phase-contrast method. *Mon. Not. R. Astron. Soc.* **94**, 377–384 (1934).

40. Tkachuk, A. *et al.* X-ray computed tomography in Zernike phase contrast mode at 8 keV with 50-

nm resolution using Cu rotating anode X-ray source. *Zeitschrift fur Krist.* **222**, 650–655 (2007).

41. Chen, Y.-T. *et al.* Hard x-ray Zernike microscopy reaches 30 nm resolution. *Opt. Lett.* **36**, 1269 (2011).

42. Douissard, P.-A. *et al.* A versatile indirect detector design for hard X-ray microimaging. *J. Instrum.* **7**, P09016–P09016 (2012).